Title
Design and Optimization of Collocated Dual Stage Actuated Suspensions in Hard Disk Drives Using Finite Element Analysis

Author
Wang, Yangfan

Publication Date
2015

UNIVERSITY OF CALIFORNIA, SAN DIEGO

Design and Optimization of Collocated Dual Stage Actuated Suspensions in Hard Disk Drives Using Finite Element Analysis

A thesis submitted in partial satisfaction of the

requirements for the degree Master of Science

in

Engineering Sciences (Mechanical Engineering)

by

Yangfan Wang

Committee in Charge:

Professor Frank E. Talke, Chair
Professor Vlado Lubarda
Professor Alison L. Marsden

2015

The thesis of Yangfan Wang is approved, and it is acceptable in quality and form for publication on micro film and electronically:

____

____

____

Chair

University of California, San Diego

2015

DEDICATION

To my parents, Xianjie Wang and Yin Xie

TABLE OF CONTENTS

LIST OF FIGURES

LIST OF TABLES

ACKNOWLEDGEMETNS

First and foremost, I would like to express my most sincere gratitude to my advisor Professor Frank E. Talke for his continuous support and guidance. I would like to thank him for his encouragement and valuable advice for my research. I greatly enjoyed working in his Lab.

Secondly, I would like to thank John Hogan and Hanya-san of NHK for their interest and support of this study.

In addition, I would like to thank the members in Professor Talke's research Lab, who helped me throughout my graduate studies. In particular, I would like to thank Dr. Longqiu Lee and Karcher Morris for helping me with the collocated dual stage actuator project. I would like to thank my officemate Youyi Fu for the countless discussions and fruitful conversations. I am grateful to all other lab members at the Talkelab, Young Woo Seo, Tan Trinh, Alex Phan, Liane Mattes, and Benjamin Suen for their help and friendship.

Furthermore, I would like to acknowledge Professor Vlado Lubarda for his valuable suggestions in every group meeting. In addition, I want to thank Professor Alison Marsden for the great lectures in fluid dynamics and numerical methods classes.

Finally, I would like to thank my parents, Xianjie Wang and Yin Xie, for their constant mental and financial support during my time in the United States.

Acknowledgement for published work:

Chapter 3 and Chapter 4, in part, is a reprint of the material as it appears in “Design and Optimization of Collocated Dual Stage Suspensions”, Yangfan Wang, Longqiu Li, Karcher Morris, John Hogan, Frank E. Talke, submitted to Microsystem Technologies, 2014. The dissertation author was the primary investigator and author of this paper.

ABSTRACT OF THE THESIS

Design and Optimization of Collocated Dual Stage Actuated Suspensions in Hard Disk Drives Using Finite Element Analysis

by

Yangfan Wang

Master of Science in Engineering Sciences (Mechanical Engineering)

University of California, San Diego, 2015

Professor Frank E. Talke, Chair

Higher performance suspensions are necessary to obtain ultra-high magnetic areal density in hard disk drives (HDDs). Currently suspension-based dual stage actuated (DSA) designs utilize two piezoelectric actuators placed at the base of the suspension, allowing for a secondary input that can respond to undesirable off-track motion. Collocated designs are a probable DSA alternative. The design of a collocated head-based dual stage actuator is investigated using finite element analysis. The effect of

gimbal design dimensions on the lateral deflection of the read-write element is evaluated. The resonant frequency response and stress distribution are studied. A comparison of the proposed dual stage head-based actuator is made with other suspension-based designs and the collocated design proposed by Lengert et al.[1]. Guidelines for optimization of the designs are presented and discussed.

1 Introduction

Chapter 1 explores the history and the main components of magnetic recording hard disk drives. Additionally, basic principles of magnetic recording and emerging technologies are introduced.

1.1 History of Magnetic Recording Hard Disk Drives

The computer industry has developed rapidly since the 1940's, creating an increasing demand for digital data storage over the years. Because of the advantages of high-capacity and fast accessibility, magnetic recording hard disk drives (HDDs) have become one of most important computer components for digital data storage since the 1950's.

Figure 1: IBM Random Access Memory Accounting Machine (RAMAC)[2]

In 1956, International Business Machines (IBM) Corporation introduced the Random Access Memory Accounting Machine (RAMAC), which can be considered as the first computer hard disk drive. The RAMAC contained fifty 24 inch diameter iron-oxide-coated aluminum disks. The disks rotated at 1200 revolutions per minute (RPM). The RAMAC had a total capacity of 5 megabytes (MB) and a data transfer rate of 8.8 kilobytes per second (KB/s). The areal density was about 2000 bits per square inch (2Kbit/ $inch^2$). The flying height of the slider over the disk was around 25 µm.[2]

In 1961, IBM introduced the 1301 series disk drive with a total capacity of 25 MB. The implementation of hydrodynamic air bearing successfully reduced the minimum flying height of the slider to 6 µm. The improved model 1302 was introduced two years later, which further increased the capacity up to 4 times compared to model 1301. Another milestone of the HDD industry was the introduction of the IBM 3340 series HDD in 1973. The IBM 3340 featured a much smaller flying height of 0.5 µm. This advanced head and disk technology was known as "Winchester Technology". Back in the 1960's and 1970's, HDDs were large in size, and extremely expensive. Only government agencies, supercomputing centers, and airline companies could afford the use of computer hard disk drive systems.[2]

Today, hard disk drives use generally 2.5 inch diameter disks for laptops and 3.5 inch diameter disks for desktop computers. The rapid development of the personal computer created a large demand for affordable, high-capacity and small form factor hard disk drives. Continuous technology improvements have been developed for the HDDs to meet the need for data storage. Today, the increasing demand for cloud computing and cloud storage for large data centers is accelerating the development of hard disk drives more than ever.

The areal storage density is the most important factor of the hard disk drives. The first computer hard disk drive RAMAC had a capacity of 5MB and an areal storage density of 2000 bits per square inch (2000bit/ inch^2). In 2014, Seagate Technology shipped the world's first 8 TB (1 Tbyte=10^{12} bytes, with 1 byte=8bits) HDD with an areal density of nearly 1 Tbit/inch^2[3]. This represents a nearly 500 million-fold increase in areal storage density over 58 years. Figure 2 shows the development roadmap of HDD products versus flash products.[4]

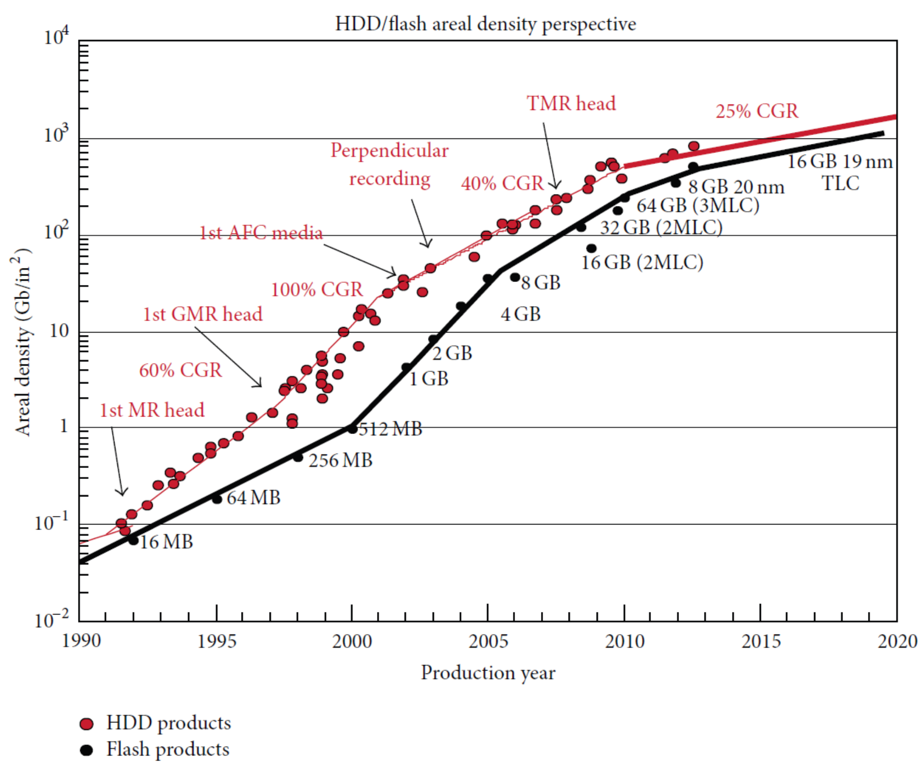

Figure 2: Areal Density roadmap for HDD and Flash products

1.2 Hard Disk Drive Components

Figure 3 shows the major components of a modern hard disk drive. One or more magnetic hard disks are mounted on a hub driven by a spindle and rotating at speeds between 5,000 revolutions per minute (RPM) and 15,000 revolutions per minute (RPM). The data on the disks is accessed by read/write elements incorporated in the sliders. As the disks rotate, the sliders “fly” at a constant height above the disks. The slider is mounted on a suspension arm that is controlled by a voice coil motor (VCM). The suspension arm has a radial motion over the disk surface which provides fast random accessibility to the data on the disk.

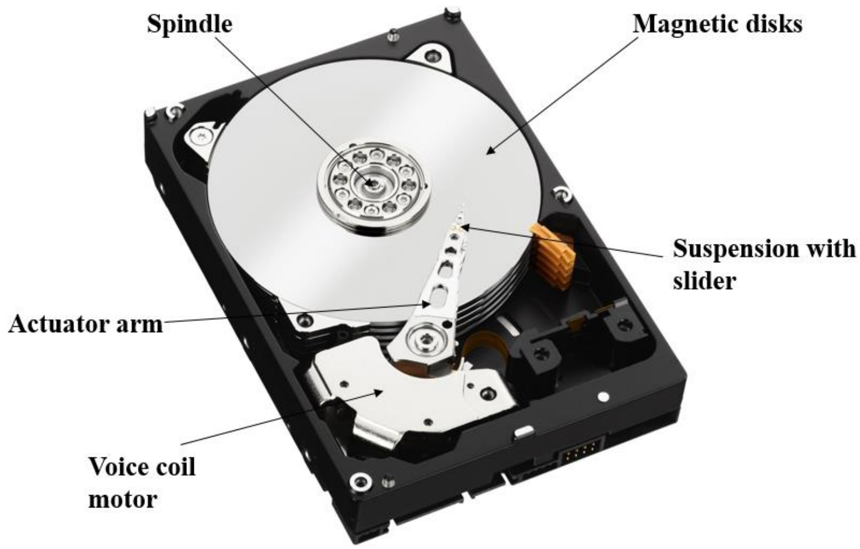

Figure 3: A modern hard disk drive, with major components[5]

1.2.1 Air Bearing Sliders

The air bearing slider in a hard disk drive is typically made of alumina titanium carbide (Al_2O_3-TiC). The air bearing slider carries the magnetic read/ write element on the trailing edge. When flying above the disk, the slider is supported by an air bearing, which is generated as a result of the viscous shear between the slider surface and the rotating disk surface.

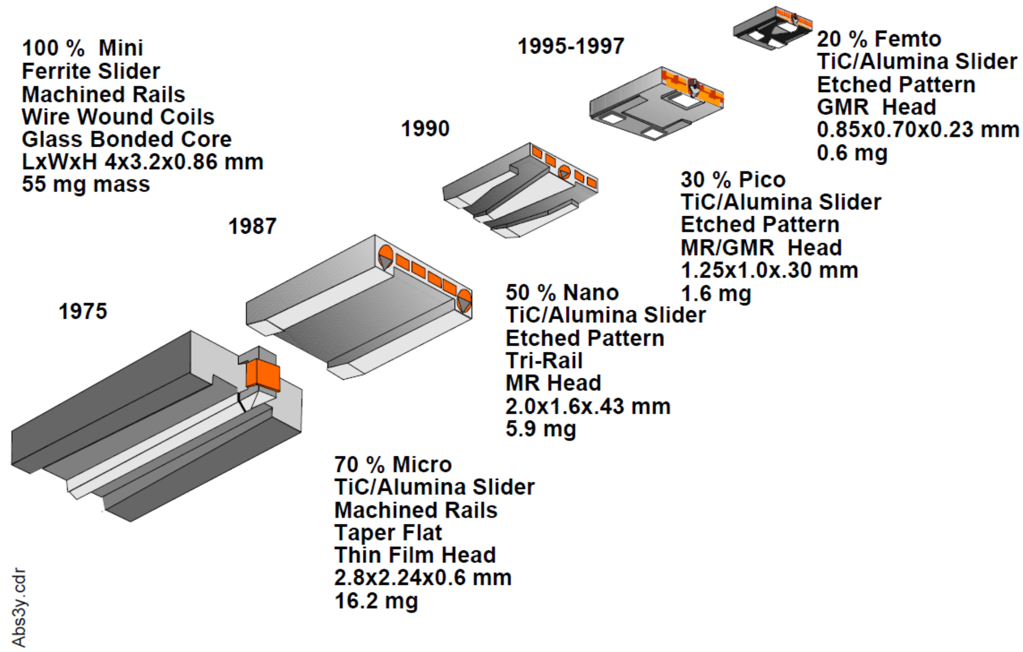

Figure 4: Evolution of air bearing slider design[6]

Figure 4 shows the evolution of air bearing designs from 1975 to today. The air-bearing surface (ABS) of the slider refers to its bottom side facing the disk surface. Through the years, the air bearing slider size has been decreased and air bearing surface geometry has become more and more complex. The 1975 “mini” ferrite slider had dimensions of 4mm, 3.2mm, and 0.86mm for length, width and height, respectively. Today, the pico and femto form factor sliders are the most common ones in HDDs. The dimensions of the pico slider are 1.25mm, 1.0mm, and 0.3mm. The dimensions of the femto slider are even smaller, i.e., 0.85mm, 0.7mm, and 0.23mm. They are both sub-ambient pressure slider designs. The first sub-ambient pressure air bearing slider was introduced in the 1990’s. Figure 5 shows a sub-ambient pressure air bearing surface design. The sub-ambient pressure air bearing surface has recessed areas, the so-called cavity, which is a reverse step in the bearing. The cavity reduces the total load on the air bearing generated by the positive pressure regions. This is designed to allow the sliders to obtain constant flying height near the inside diameter and outside diameter of a disk. In today's hard disk drives, air bearing surfaces are designed to maintain an extremely low but constant flying height independent of disk position and ambient pressure. Photolithography and etching techniques are the most common manufacturing methods.[6]

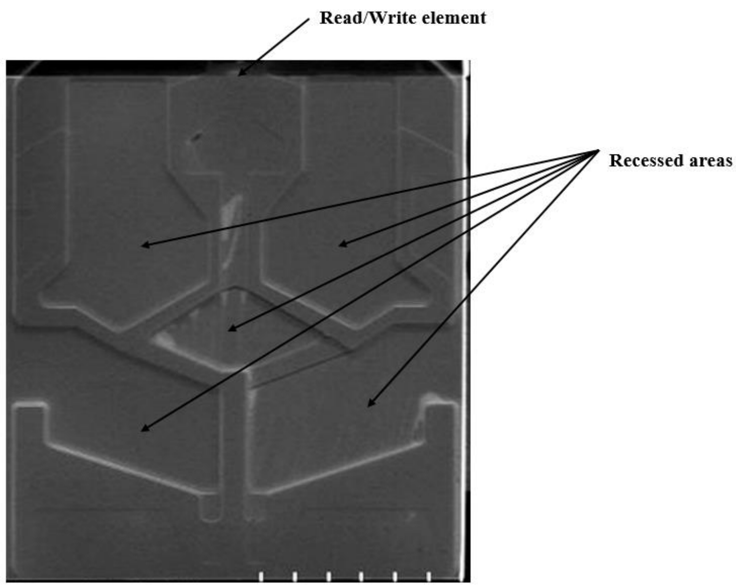

Figure 5: An air bearing surface from Western Digital Technology, Inc.[5]

In order to increase areal density, the flying height reduction plays an important role. Reducing the flying height results within a decrease in the magnetic spacing. The magnetic spacing influences the reading and writing of magnetic information. To keep up with the increasing areal storage density and the reducing size of air bearing slider design, thermal flying-height control (TFC) sliders were recently developed to reduce the flying height of the head disk interface.[7] TFC sliders incorporate a thin film resistance heater that can be energized in order to change the geometry of the air bearing surface near the read/write element, thereby controlling the spacing at the interface.[8] Figure 6 shows a schematic of a read/write protrusion at the tip of the air bearing slider. As a result, the flying height has been reduced from 25 µm (RAMAC, 1956) to 1-2 nm today, with the help of TFC technology.

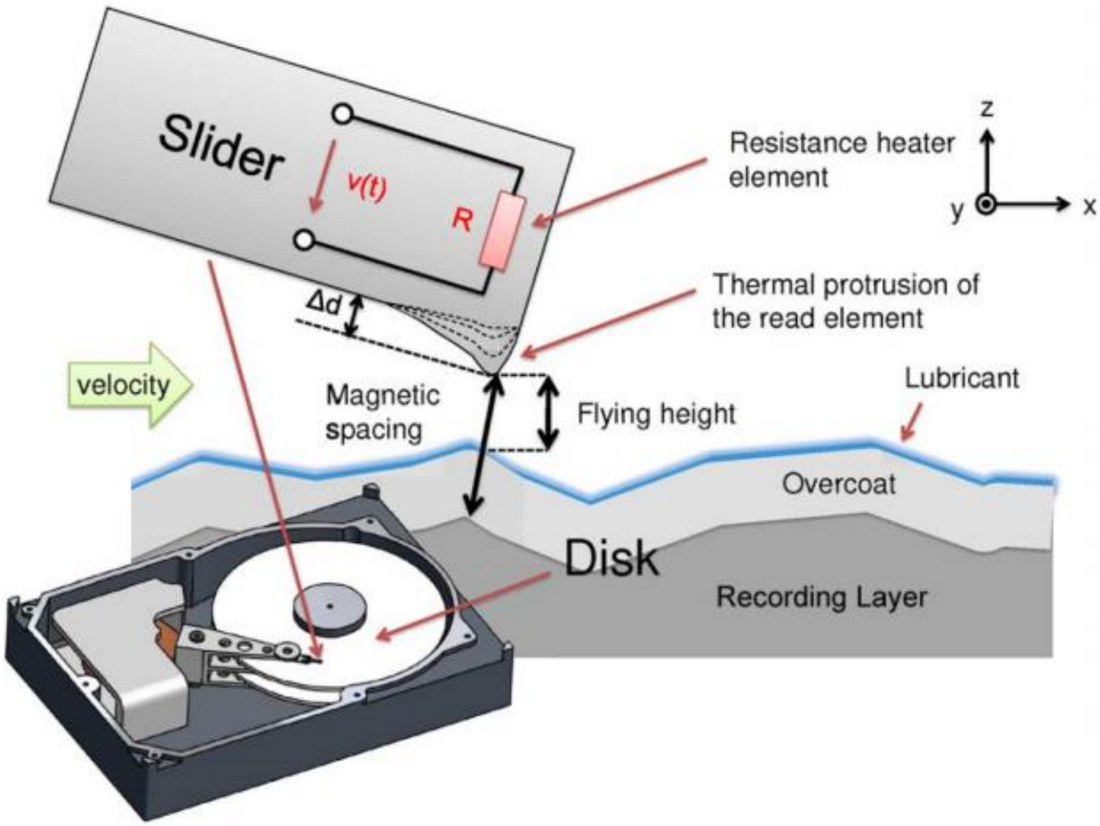

Figure 6: Schematic of a read/write protrusion in the slider[9]

1.2.2 Suspensions

Figure 7 shows the assembly of slider, gimbal and suspension. The slider body is mounted on the flexure/gimbal and then attached to the suspension loadbeam. The suspension can hold the slider to a relative stable flying height. In terms of lateral motion, the suspension can also provide sufficient stiffness to ensure accurate and rapid lateral response. The suspension positions the slider over the disk surface and provides pre-load on the slider. When flying above a disk, the slider presses against the dimple on the suspension to allow pitch and roll motions.

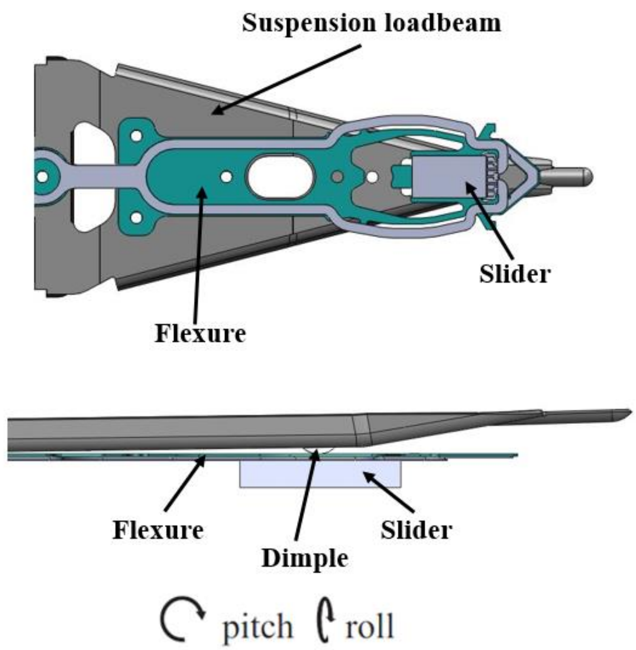

Figure 7: Suspension Assembly, front view (top); side view (bottom)

Figure 8 shows the evolution of typical suspension designs. Following the same trend as for slider, the suspension size has reduced from 25 mm to less than 10 mm over the years.

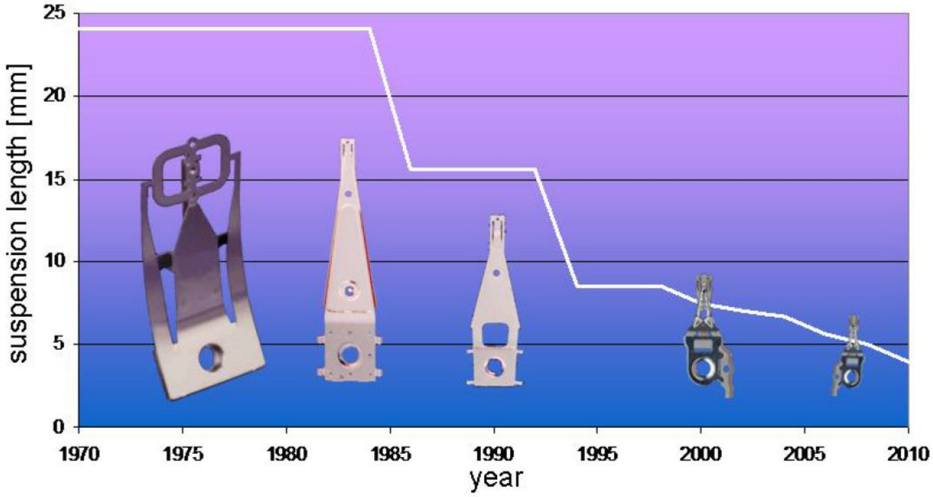

Figure 8: Evolution of suspension designs[10]

1.2.3 Magnetic Disks

The magnetic disks have a multilayer structure as shown in Figure 9. The substrate layer of a disk is usually made of aluminum or glass. For a glass disk, the magnetic layer is directly deposited on the glass layer. For an aluminum disk, a nickel phosphorous underlayer is deposited on the disks before the magnetic layer. The magnetic layer is generally made of a 15-50 nm thick film cobalt alloy. The magnetic layer provides the storage medium. The fabricating methods of the magnetic layers are usually sputtering or chemical vapor deposition (CVD). The magnetic layer is then covered by a diamond-like-carbon (DLC) overcoat to protect the surface from wear. On top of the DLC layer is a thin lubricant layer.

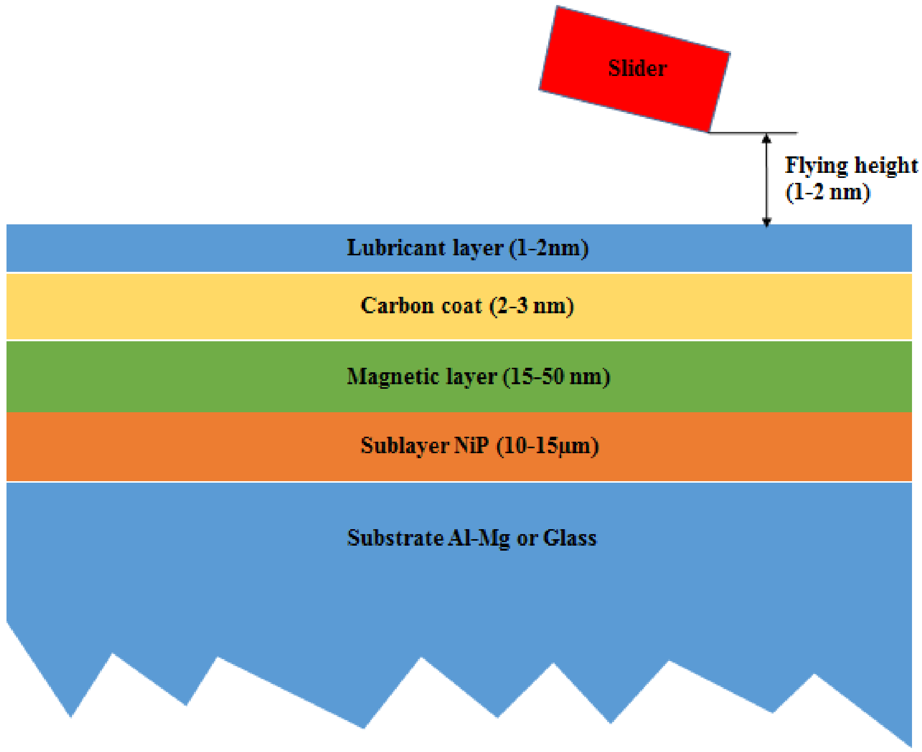

Figure 9: Multi-layer structure of a magnetic disk

1.2.4 Head/Disk Interface

The interface between the air bearing slider and the rotating hard disk is called the head/disk interface. The relative head disk spacing is maintained by the pressure distribution on the air bearing surface. The pressure on the air bearing surface is in balance with the viscous shear in the air film. The air flow between the slider and the disk surface can be expressed using the so-called Reynolds equation.[11] The Reynolds equation is derived from the Navier-Stokes equation. For two dimensional compressible, laminar flow and constant viscosity gases, the basic equation is given as following:

$$\frac{\partial}{\partial x}(\bar{Q}ph^3)\frac{\partial p}{\partial x}+\frac{\partial}{\partial y}(\bar{Q}ph^3)\frac{\partial p}{\partial y}=6\mu(U\frac{\partial ph}{\partial x}+V\frac{\partial ph}{\partial y})+12\mu\frac{\partial ph}{\partial t} \tag{1.1}$$

, where U and V are the velocity components in x and y direction, p is the local pressure, h is the spacing, and μ is the viscosity of air. This second order partial differential equation can be solved using finite element or finite difference methods. For extremely low flying height, so-called rarefaction effects must be considered. $\overline{Q}(Kn)$ is a factor that is a function of the Knudsen number $Kn = \lambda / L$, where λ is the mean free path of the gas molecules and L is the characteristic length.[12],[13] The modified Reynolds equation is shown in equation 1.2. However, when the flying height reaches the atomic level, intermolecular adhesion force should be taken into consideration.[14]

$$\frac{\partial}{\partial x}(\overline{Q}(Kn)ph^3)\frac{\partial p}{\partial x} + \frac{\partial}{\partial y}(\overline{Q}(Kn)ph^3)\frac{\partial p}{\partial y} = 6\mu(U\frac{\partial ph}{\partial x} + V\frac{\partial ph}{\partial y}) + 12\mu\frac{\partial ph}{\partial t} \qquad (1.2)$$

1.3 Principle of Magnetic Recording

Magnetic recording is based on the theories of magnetism and electromagnetism. Figure 10 shows the principle of longitudinal magnetic recording. For the write head to write a bit on a magnetic layer, an external magnetic field is applied. The magnetic field is created by an inductive write head. Digital information is coded as magnetic transitions between bits. During writing, the data are sent in binary form (0's and 1's). The data are then converted into a current in the conductive coils of the write head. The current through the coil generates a magnetic field at the gap. The field at the pole tip passes through the medium, thereby aligning the magnetization of a bit. Depending on the direction of the current, two distinct magnetization directions can be written on the disk.

Figure 11 shows the schematic of the principle of perpendicular magnetic recording. The magnetization are in vertical direction, thus increase the areal storage density.

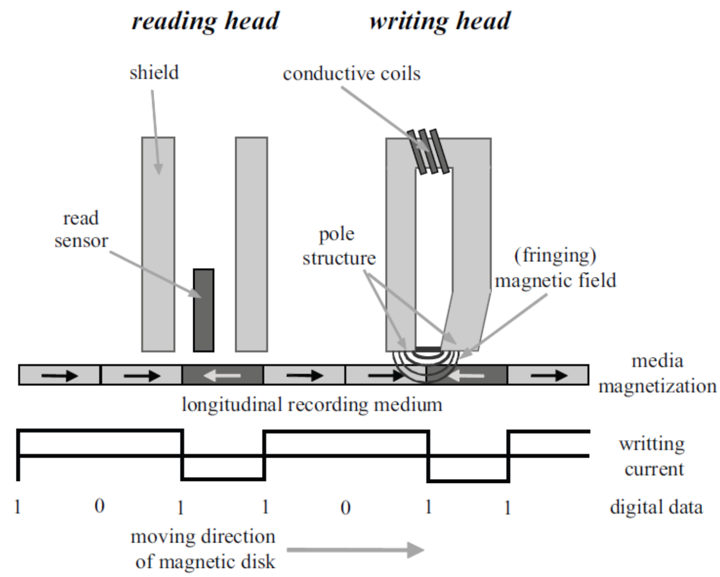

Figure 10: Schematic of the principle of longitudinal magnetic recording[15]

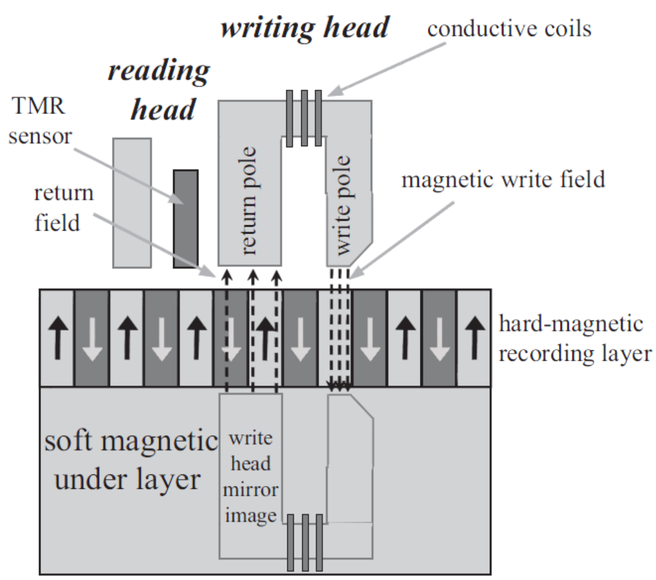

Figure 11: Schematic of the principle of perpendicular magnetic recording[15]

For reading the data from the disk, the read head detects the change in the magnetic field of adjacent bits and converts this change into an electrical signal. The signal is then converted into binary information that is sent to the computer for processing.

1.4 Emerging Technology in HDDs

The driving force for HDD evolution is to improve areal storage density in order to achieve higher capacity. The super-paramagnetic effect and the signal-to-noise ratio are considered as two major constraints that are preventing the areal density from growing. The heat assisted magnetic recording (HAMR) technology has the potential to solve the super-paramagnetic effect. And bit patterned media technology can eliminate much of the signal-to-noise ratio problem. These technologies are introduced in this section of the thesis.

1.4.1 Helium Technology

Helium has only one-seventh the density of air. Reducing friction from the spinning disks lowers the electrical power consumed by the HDD. It also allows for smaller spacing between disks increase the number of disks in one drive. In 2014, HGST pronounced the first helium HDD, with a seven-disk, 6 TB helium drive with the same physical size as the common five-disk, air filled HDD. This drive consumes 23% less power. However, sealing of the HDD can be one of the difficulties in manufacturing helium drives.[6] Figure 12 shows the z-height comparison between a conventional 5-disk 4TB drive and the 7-disk 6 TB helium Drive.

Figure 12: Size comparison between a Helium 7-disk HDD and an air 5-disk HDD[6]

1.4.2 Bit Patterned Media (BPM)

In Bit Patterned Media (BPM) recording, the information is stored in single "island" structures on the disk surface. In Figure 13, the bits are physically separated by a lithographic process, one island represents one bit, eliminating transition noise in the radial and the circumferential direction of the disk. Richter et al.[16] showed the BMP technology could increase the areal density up to 5 Tbits/inch^2. One challenge is nano-lithography. Cost effective manufacturing technologies need to be developed. Another downside of BPM is the intensive processing of disk surface may compromise head/disk interface and magnetic spacing.

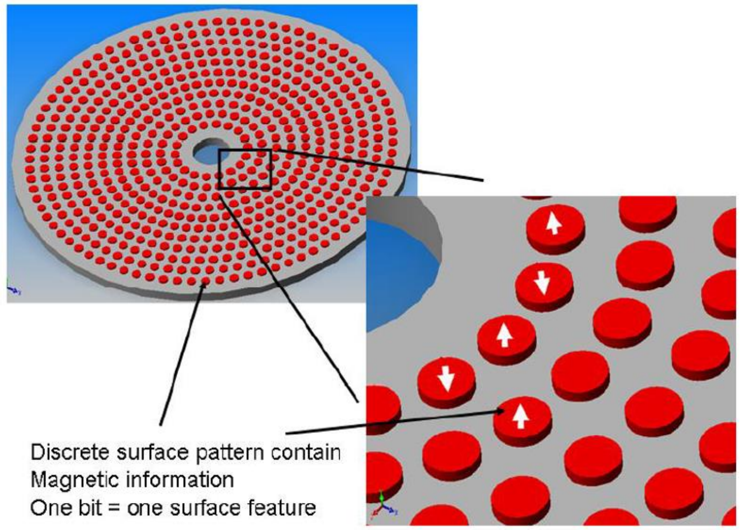

Figure 13: Schematic of bit patterned media[14]

1.4.3 Heat Assisted Magnetic Recording (HAMR)

Heat Assisted Magnetic Recording (HAMR) uses a small laser to heat the part of the disk that one wants to write on. (Figure 14) In this approach, a high coercivity magnetic material is used to increase the magnetic energy of a single bit. The coercivity decreases with increasing temperature as shown in Figure 15. The heat changes the coercivity of the disk for a short time, reducing the super-paramagnetic effect while writing takes place. During the cooling, the desired magnetization is frozen in the bit cell. HAMR allows writing on a much smaller scale than before, increasing the areal storage density on a standard disk platter. However, the challenges include the development of an integrated optical and magnetic write-head; Elevated temperatures in the head and medium accelerating the failure of the drive.

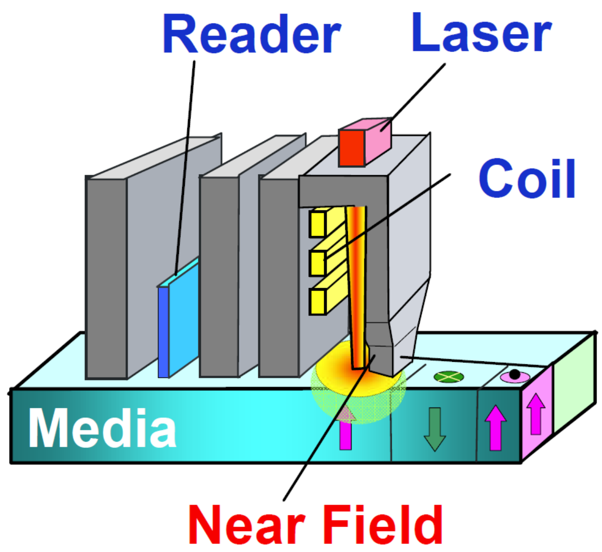

Figure 14: Schematic of heat assisted magnetic recording (HAMR)[6]

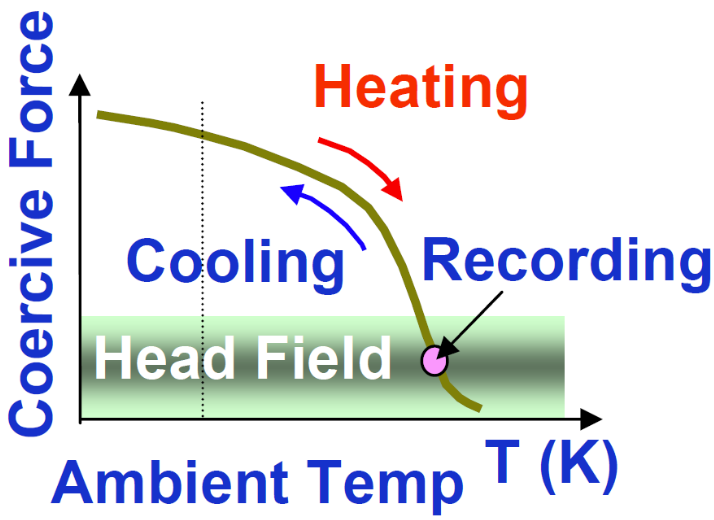

Figure 15: Schematic of write process in HAMR[6]

1.5 Thesis Organization

This dissertation focuses on the design and optimization of collocated dual stage actuated (DSA) suspensions in hard disk drives (HDDs) using finite element analysis (FEA).

Chapter 1 introduces hard disk drives with a brief description of magnetic recording history along with a description of major advances and the components in HDDs. The basic scientific principles used to overcome challenging obstacles in magnetic recording industry, as well as recent/future technology in HDDs are discussed.

Chapter 2 provides an overview of both suspension based and collocated DSA designs.

Chapter 3 explores various collocated DSA HGA designs and the finite element model set ups.

Chapter 4 presents the simulation results of the trailing edge lateral deflection, frequency responses, and stress distributions.

Chapter 5 is a conclusion of this dissertation.

2 Collocated Dual Stage Actuated Suspensions in Hard Disk Drives

In chapter 2, the suspension's use of piezoelectric elements as second stage actuators was introduced. The advantages and disadvantages of both suspension-based and collocated DSAs are discussed.

2.1 Dual Stage Actuated (DSA) Suspensions

The capacity of a single hard disk drive has increased dramatically since the RAMAC (IBM, 1956). As the areal density increases, the spacing between tracks shrinks. Narrower track spacing increases the difficulty of positioning the read/write element over the center of the data track. The voice coil motor (VCM) has a limited bandwidth due to its inertia. Off-track motion can be caused by the sway motion of the suspension arm.

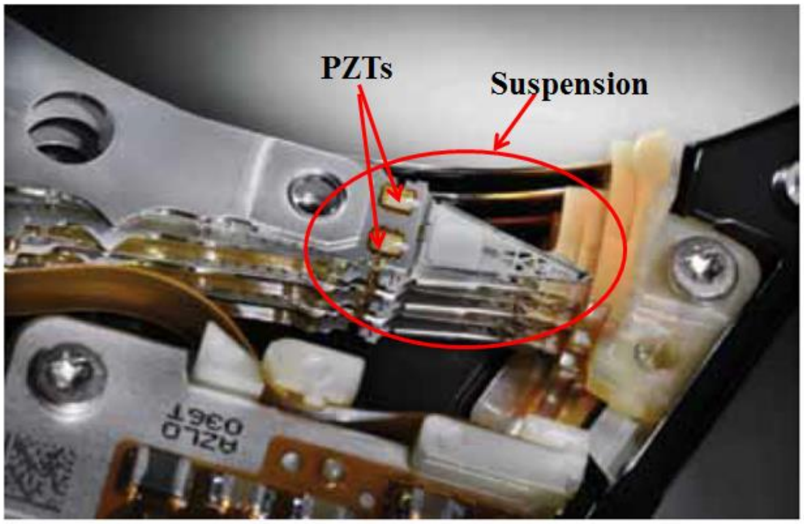

Figure 16: A close look at the typical suspension-based DSA[6]

Conventional HDDs use the VCM as a single stage actuator. During the radial movement of the suspension arm, the motion extends from the VCM to the read/write head, which could cause track mis-registration (TMR) of the read/write head over the high density tracks. To minimize these off-track motions, some high performance HDDs use piezoelectric elements lead zirconate titanate (PZT) as second stage actuators in addition to the VCMs to meet higher accuracy and speed [17].

Compared to a single stage suspension, dual stage actuated suspensions (DSA) provide a higher bandwidth and better positioning accuracy. Figure 16 shows a close-up picture of a typical suspension-based DSA product. DSAs can be classified into ‘‘suspension-based’’ and “collocated” dual stage designs. In a suspension-based design, piezoelectric elements (PZTs) are mounted at the base of the suspension while in a collocated design one or more PZTs are located close to the head, ideally ‘‘collocated’’ with the head.

2.2 Piezoelectric Materials

Piezoelectricity is the electric charge that accumulates in certain solid materials in response to applied mechanical stress. The piezoelectric effect refers to the linear relationship between the mechanical and the electric state in crystalline with no inversion symmetry.[18] The piezoelectric effect is a reversible process. When the material is deformed, a voltage change is observed. When applying a voltage to the material, mechanical stress is be generated. Lead zircronate titanate (PZT) with chemical formula $Pb[Zr_xTi_{1-x}]O_3$ ($0<x<1$) is used for dual stage actuator piezoelectric material. The working principle of PZT material is explained in Figure 17. When a voltage applied along the thickness of the material, the deformations in all three directions can be calculated using the equations 2.1 to 2.3.

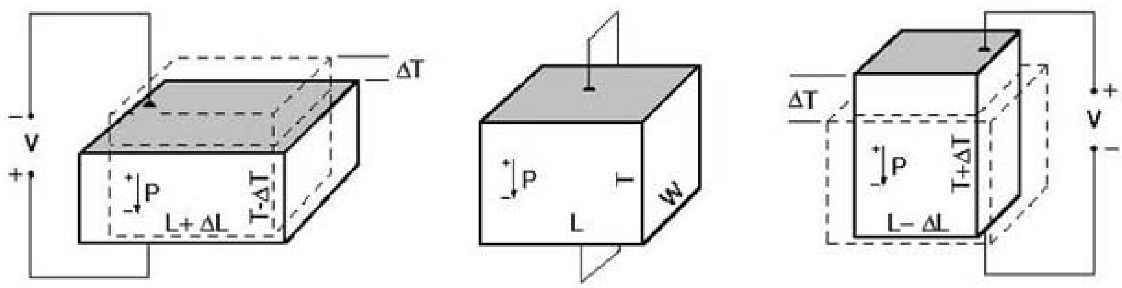

Figure 17: Working principle of piezoelectric material[19]

$$\Delta l = d_{31} \times V \times \frac{l}{t}, \quad (2.1)$$

$$\Delta w = d_{31} \times V \times \frac{w}{t}, \quad (2.2)$$

$$\Delta t = d_{33} \times V, \quad (2.3)$$

where Δl, Δw, Δt represent change of length l, width w, and thickness t, respectively. d_{31} and d_{33} are piezoelectric constants. V is applied voltage.

2.3 Suspension Based DSA

Modern high density HDDs are implementing suspension based DSA to improve track performance. Figure 18 shows a suspension baseed DSA design. The PZTs are positioned at base of the suspension, connected to the loadbeam with adhesive layers. The dimensions of each PZT in this case are 1.40mm, 1mm, and 0.1 mm for the length, width, and thickness, respectively. The two PZTs are oppositely polarized. When a voltage is applied, one PZT contracts while the other one extends, generating a rotary motion of the head showing in Figure 19.

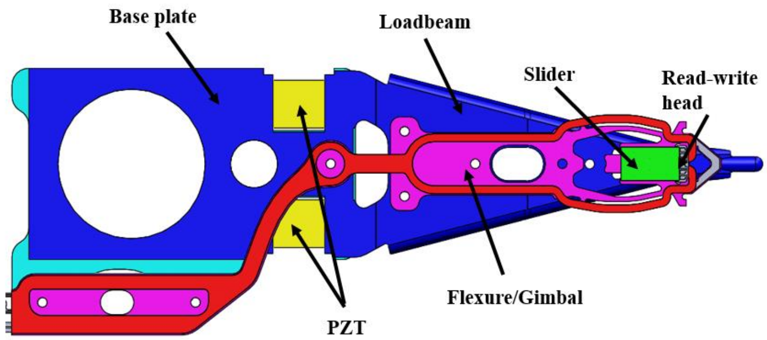

Figure 18: Top view of suspension-based DSA

Similar to the single stage actuator, the lateral deflection is linearly related to the distance between the read/write head and PZTs. This radial motion is used to correct track mis-registration with the track center. Compared to the collocated DSA, the magnitude of lateral deflection is significantly larger. But a large deflection reduces the accuracy of head positioning and the natural frequencies. Therefore, HDD and suspension companies are currently researching and developing the collocated DSA to achieve a better track performance. A number of different DSA designs have been investigated in the recent past. Mori et al.[17] provided a dual stage actuator in which a PZT actuator is mounted in the load beam. The static and dynamic characteristics of their design were investigated. Evans and Griesbach[20] presented a suspension based piezoelectric actuator design. Lau and Du[21] proposed several new suspension-based DSA designs and studied how to improve the stroke while keeping high torsional frequencies. Boettcher et al.[22] presented a discrete-time modeling algorithm based on frequency response function measurements and compared the performance of two different dual stage controllers. Liu[23], [24] presented a circuit model and a dynamic model for a DSA.

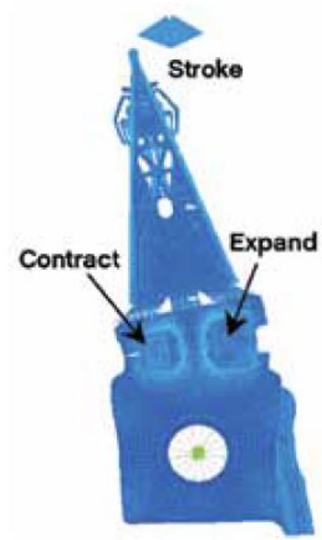

Figure 19: Rotary motion cost by PZTs[6]

2.4 Collocated DSA

In Figure 20, a design of a collocated DSA is shown, using two PZTs located on each side of the read/write head. Compared to the suspension-based DSA, the collocated DSA is more desirable in terms of the accuracy of head position and frequency response. The difficulty is to overcome the smaller later deflection.

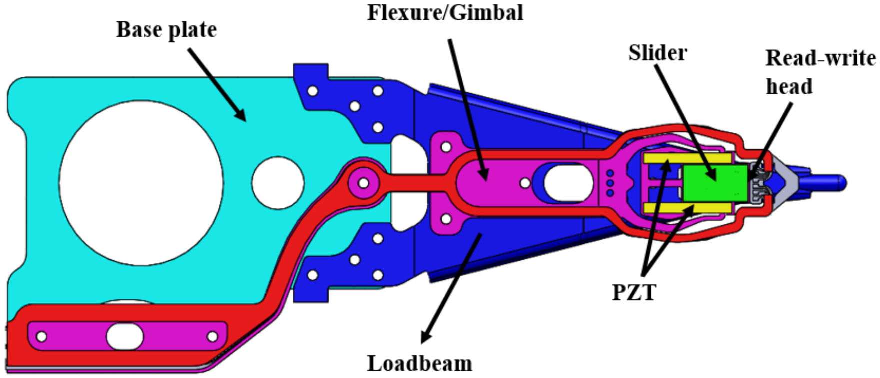

Figure 20: Top view of collocated DSA

In later chapters of this dissertation, a novel collocated DSA design is proposed. Finite element analysis is employed to investigate the stroke of the suspension and the static and dynamic performance as a function of the gimbal design dimensions. A comparison of the present results with other DSA designs is made. Guidelines for optimization of the designs are presented and discussed.

3 Collocated DSA Designs and Finite Element (FE) Models

In chapter 3, various collocated DSA HGA designs are explored. Thermal piezo-electric analogy is used for analyzing the PZT material. A finite element model is set up and design parameters are explained.

3.1 Collocated DSA Designs

With an advantageous moment arm between the PZTs and the head, suspension-based DSAs have traditionally had a larger lateral stroke compared with collocated DSAs in which the PZTs are very close to the head. Only a few papers have dealt with collocated DSAs. Jing et al. [25] proposed a U-type DSA based on two thin film PZTs which were used to control the slider directly. Lengert et al.[1] investigated a collocated DSA design to study the stroke sensitivity using finite element analysis.

3.1.1 Previous Design

In Lengert's design, shown in Figure 21, a single PZT was placed behind the slider with dimensions of 0.85mm, 0.35mm, and 0.1mm of length, width, height, respectively. The motion of the head was calculated using a thermal analogy to the piezo-electric effect. When a voltage is applied to the PZT, expansion will occur in the x and y direction while a contraction will occur in the z direction. As shown in Figure 22, the mounting pad connections A and B on the gimbal are asymmetric with respect to the horizontal centerline of the PZT. When the PZT expends or contracts, a rotary motion will be observed. Figure 22 shows the design parameters of this collocated DSA model.

In his design, a lateral deflection of 3-5 nm/V was observed. The current suspension-based DSA suspensions normally a the lateral deflection on the order of 20nm/V. In order to compete with the suspension-based DSA, new collocated designs need to be developed to overcome the insufficient lateral deflection.

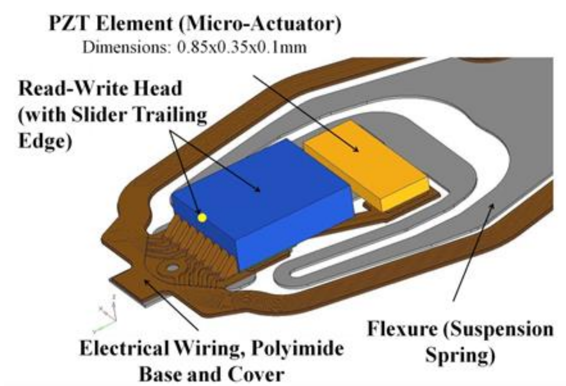

Figure 21: Single PZT collocated flexure-based suspension design[1]

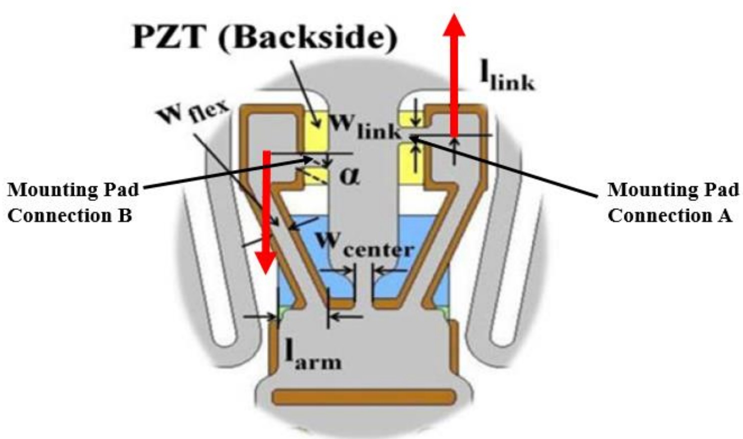

Figure 22: Operating principle of collocated suspension[1]

3.1.2 New Designs

The geometries of the models were first created in SolidWorks, a 3D modeling computer aided design software. In order to simulate the read/write head lateral deflection, only the head gimbal assembly (HGA) is modeled to save computational cost in the finite element analysis. Three different DSA designs with two separate PZT elements are proposed in Figure 23.

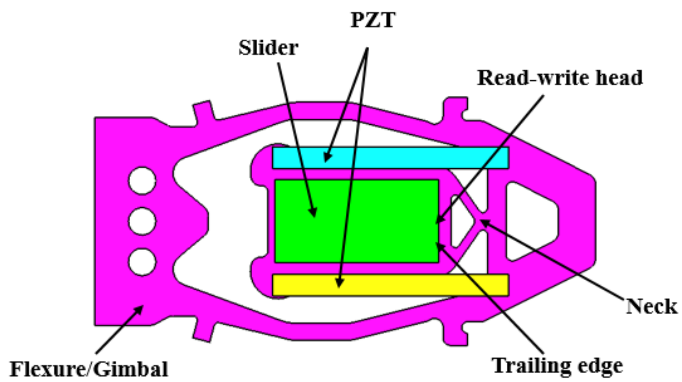

(a) Design 1

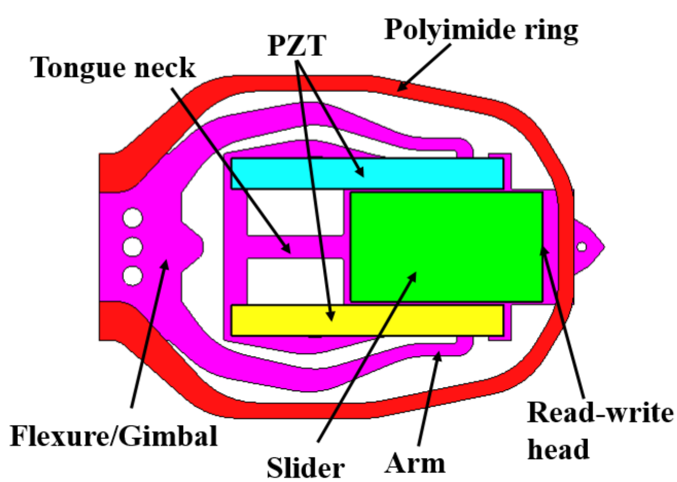

(b) Design 2

Figure 23: (a) Design I: Head-gimbal assembly of new collocated DSA.

(b) Design II. (c) Design III

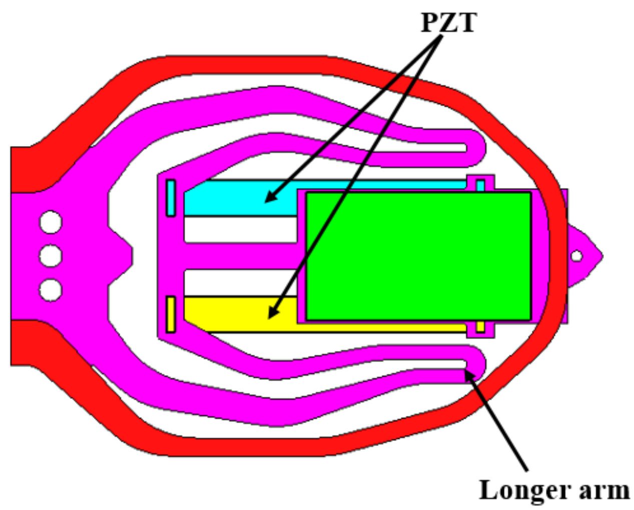

(c) Design 3

Figure 23: (a) Design I: Head-gimbal assembly of new collocated DSA.

(b) Design II. (c) Design III, continued

In all three designs, the two PZTs are polarized opposite to each other and are located on the flexure tongue next to the slider. When a voltage is applied, one PZT contracts while the other one extends, generating a rotary motion of the head. In Fig. 4a, design 1 has the neck connected to the trailing edge side, while in Figure 23b (design 2) and Figure 23c (design 3), the neck is connected to the leading edge side of the head. For design 1, different neck styles have been analyzed (Figure 24). The lateral deflection of the trailing edge was only 5-7 nm/V. In order to increase the lateral deflection, the stiffness of the assembly has to be reduced.

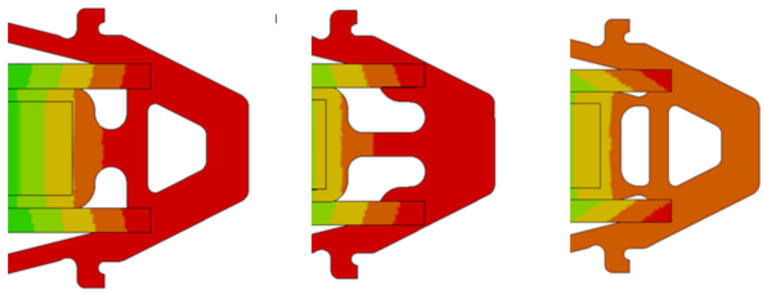

Figure 24: Various neck designs

For design 2 and 3, the two "arm" structure increases the flexibility of the assembly. In terms of lateral deflection, designs 2 and 3 have much better performance than design 1, which can reach 30 nm/V. However, the PZTs of design 3 are located on the opposite side of the read-write head limiting accessibility through the loadbeam to place the PZT which increases the difficulty to manufacture such a head. Thus, only design 2 in Figure 23b will be evaluated in this dissertation.

3.2 Finite Element Models

Finite element methods (FEMs) are numerically-based approximate methods for solving boundary value problems of partial differential equations.[26] Finite element analysis is a practical application of FEM. It is a good way for analyzing problems over complicated domains. FEA includes the use of mesh generation techniques for discretizing a continuous system into many small elements. Each element is simple to analyze by itself.

After the 3D modeling in Solidworks, the geometry was saved as an Initial Graphics Exchange Specification (IGES) file. Then, the model was imported into HyperMesh, a finite element preprocessor, for discretization and application of boundary conditions. After preprocessing in HyperMesh, the model was analyzed using LS-Dyna, a transient finite element solver. All software used is commercially available.

A thermo-structural analysis was performed to investigate the displacement of the collocated DSA design, i.e., instead of applying a current or voltage, a thermal load, in terms of temperature T, was chosen to deform the PZTs, thereby simulating the piezoelectric effect.

In this paper, we derive a numerical finite element model for the deflection of the head using the same material properties as in Lengert's study. The detailed piezoelectric material constants are listed in Table 1. The coefficient of thermal expansion can be expressed as following :

$$\Delta l = \alpha \times \Delta T \times l, \tag{2.4}$$

$$\Delta w = \alpha \times \Delta T \times w, \tag{2.5}$$

$$\Delta t = \alpha \times \Delta T \times t, \tag{2.6}$$

where Δl, Δw, Δt represent change of length l, width w, and thickness t, respectively. ΔT is change in temperature, and α is coefficient of thermal expansion. By combining equations 2.1 to 2.3 with 2.4 to 2.6, the relationship between the coefficient of thermal expansion and piezoelectric constant can be express as equations 2.7-2.9.

$$\alpha_l = \frac{d_{31}}{t}, \tag{2.7}$$

$$\alpha_w = \frac{d_{31}}{t}, \tag{2.8}$$

$$\alpha_t = \frac{d_{33}}{t}, \tag{2.9}$$

Table 1: Material properties of piezoelectric element (Lengert et al. [1])

Piezoelectric constant	
d_{33}	-7.30×10^{-10} (m/V)
d_{31}	3.30×10^{-10} (m/V)
d_{15}	7.80×10^{-10} (m/V)
Elastic compliance	
$S_{11} = S_{22}$	1.67×10^{-11} (ms^2/kg)
S_{33}	2.16×10^{-11} (ms^2/kg)
$S_{44} = S_{55}$	4.04×10^{-11} (ms^2/kg)
S_{66}	4.38×10^{-11} (ms^2/kg)
S_{12}	-5.18×10^{-11} (ms^2/kg)
$S_{13} = S_{23}$	-1.04×10^{-11} (ms^2/kg)

FEA software normally does not have its own unit system. For this study, the units imported into HyperMesh are millimeter as the length unit, gram as the mass unit and second as the time unit.

3.2.1 Meshing

Figure 25 shows a meshed HGA model. The slider and two PZT elements were discretized using a 3D brick mesh with 8 node full integration. The flexure tongue and the PI cover have very small thickness; thus, they were meshed as quad shell elements. The shell elements were also using a full integrating method. The dimensions for both types of elements are 0.01 mm. The total combined element count was about 113,000.

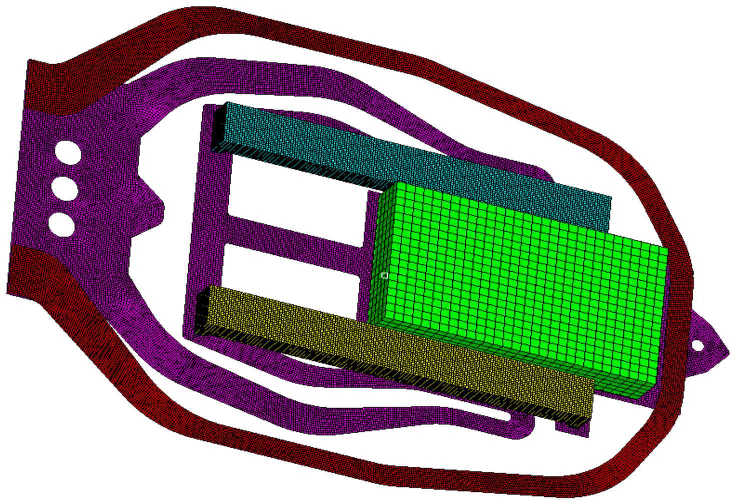

Figure 25: Meshed HGA

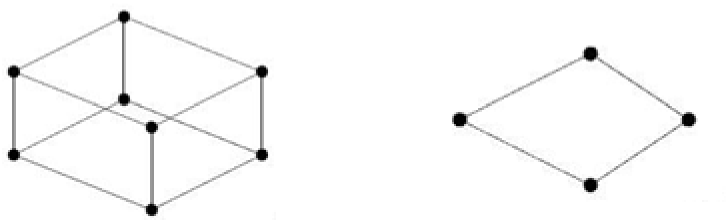

Figure 26: (Left) 8 node brick element; (Right) 4 node quad element

3.2.2 Boundary Conditions

Boundary conditions are the constraints and loads acting on particular elements. As in any finite element analysis, proper boundary conditions are crucial to the accuracy of the simulation results. The HGA model is only a portion at the tip of the whole suspension. The left edge of the assembly can be considered stationary. The nodes at the end of the flexure were fixed in all 6 degrees of freedoms (DOF), namely x, y, z, Rx, Ry, and Rz directions. When the air bearing slider is flying over the hard disk, the flying height is constant. Therefore the z-direction of the air bearing surface was fixed as the second boundary condition. One degree Kelvin (K) increase was used as the thermal load applied on the PZTs.

Between different components, the surface-to-surface contact was created on the slider/gimbal interface and PZT/gimbal interface. Contacts were evaluated using the penalty method. An implicit method is used to solve the problem.

The design shown in Figure 23b is a simplified version of the DSA suspension and does not show wiring, solder spots, welding spots or the adhesive layer between components.

3.3 Acknowledgement

Chapter 3, in part, is a reprint of the material as it appears in “Design and Optimization of Collocated Dual Stage Suspensions”, Yangfan Wang, Longqiu Li, Karcher Morris, John Hogan, Frank E. Talke, submitted to Microsystem Technologies, 2014.

4 Finite Element Analysis (FEA) Results

In chapter 4, FEA results of the trailing edge lateral deflection, whole suspension resonance frequency, and stress are presented. Guidelines for optimization of the designs are presented and discussed.

4.1 Stroke of Trailing edge for Collocated DSA Suspensions

The design parameters used in the simulations are PZT length, PZT width, PZT thickness (into the page), tongue neck length, tongue neck width, flexure tongue thickness (into the page), polyimide ring width, polyimide ring thickness, arm length and arm width. All design parameters are shown in Figure 27. All design variations were compared to a so-called "base model" with dimensions shown in Table 2.

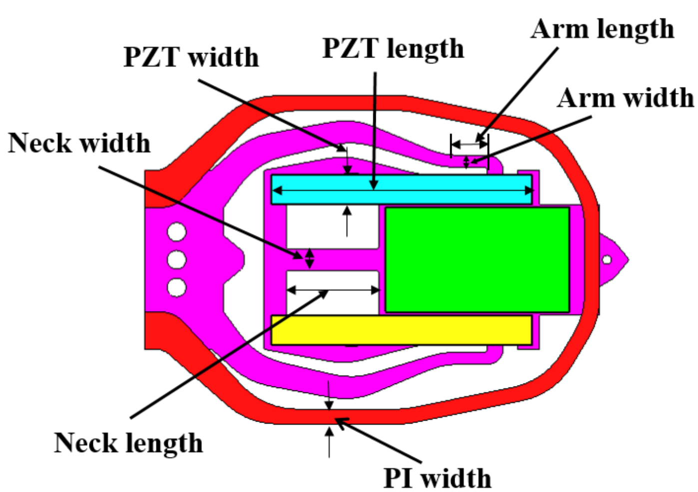

Figure 27: HGA design parameters

Table 2: “Base model” dimensions

	Length (mm)	Width (mm)	Height (mm)
PZT	1.75	0.20	0.10
Neck	0.62	0.14	0.18
Polyimide	N/A	0.10	0.01
Tongue	N/A	N/A	0.18
Arm	0.23	0.08	N/A

Figure 28 shows a resultant displacement contour plot for the base-model. A trailing edge lateral deflection of 36nm/V was obtained for the base model, which is a huge improvement from the previous single PZT design of 3-5 nm/V. For a constrained dimple case, one more constraint for fixing x and y directions was added at the dimple location. Here, a constrained dimple defines a situation where the dimple is at the center of rotation. Figure 29 shows a displacement contour plot for the constrained dimple case. A lateral deflection of 14nm/V was observed.

When the slider is flying above the disk, the relative motion between dimple and gimbal is complicated, including pitch, roll and slide motions. The main objective of this study is to see how each individual design parameter will affect the lateral deflection of the trailing edge compared to the base model. Only the unconstrained dimple case will be further discussed.

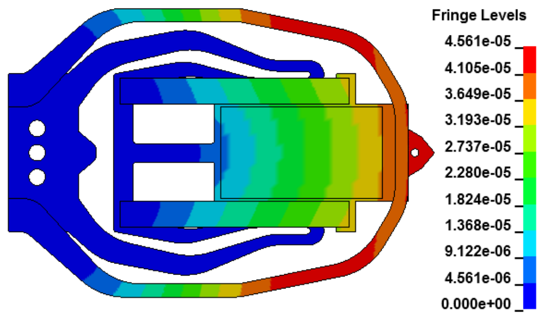

Figure 28: FEA contour plots of trailing edge deformation for base model

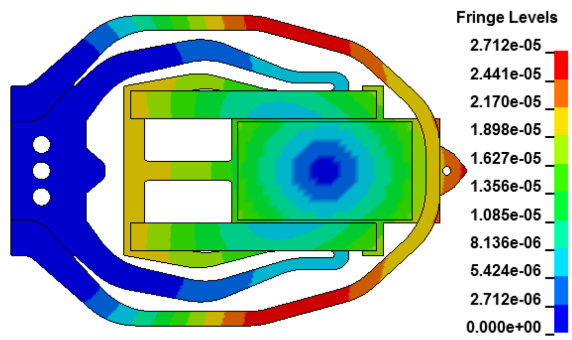

Figure 29: FEA contour plots of trailing edge deformation with constrained dimple

4.1.1 PZT Parameters

All three PZT design parameters and their comparison values are shown in Table 3. Each design parameter is compared with other four adjacent values. Base-model parameter dimensions are marked in red italic style.

Table 3: PZT design parameters dimensions

Parameter Name	**Value (mm)**
PZT Length	1.7, 1.75, *1.80*, 1.85, 1.90
PZT Width	0.10, 0.125, 0.15, 0.175, *0.2*
PZT Height	0.05, 0.075, *0.10*, 0.125, 0.15

In Figure 30a, the deflection at the trailing edge is shown as a function of the PZT length. We observe that the deflection increases from 35nm/V to 40nm/V as the PZT length increases from 1.7mm to 1.9mm. In Figure 30b, the deflection at the trailing edge is shown as a function of the PZT thickness. We observe that the deflection decreases from 70nm/V to 20nm/V as the PZT thickness increases from 0.05mm to 0.15mm. It is apparent that thinner PZTs create larger lateral deflections. In Figure 30c, the lateral deflection is shown as a function of the PZT width. We observe a slight increase in the lateral deflection if the PZT becomes wider.

According to equations 2.5 to 2.7, the coefficient of thermal expansion will change as the PZT thickness changes. Thus, a relatively large influence was observed by changing the thickness of the PZTs. When the length or width of the PZT increases, the stiffness of the PZT increases causing an increase in lateral deflection.

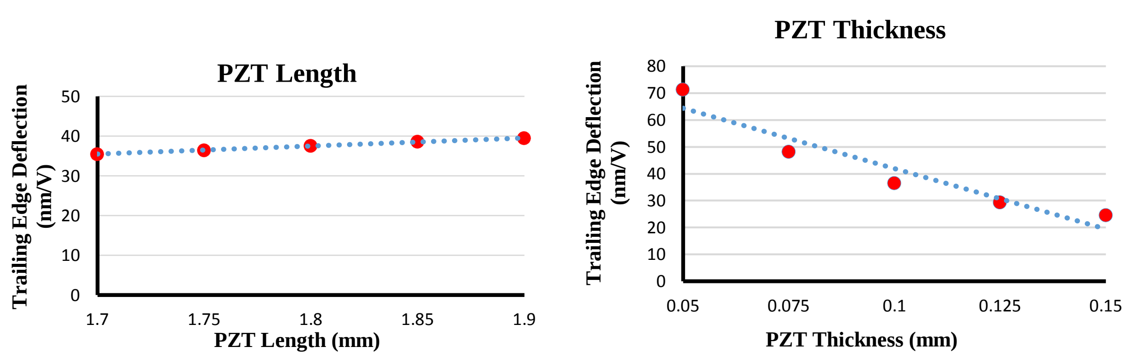

Figure 30: Lateral deflection as a function of **a)** PZT length (upper left), **b)** PZT thickness (upper right), **c)** PZT width (lower left).

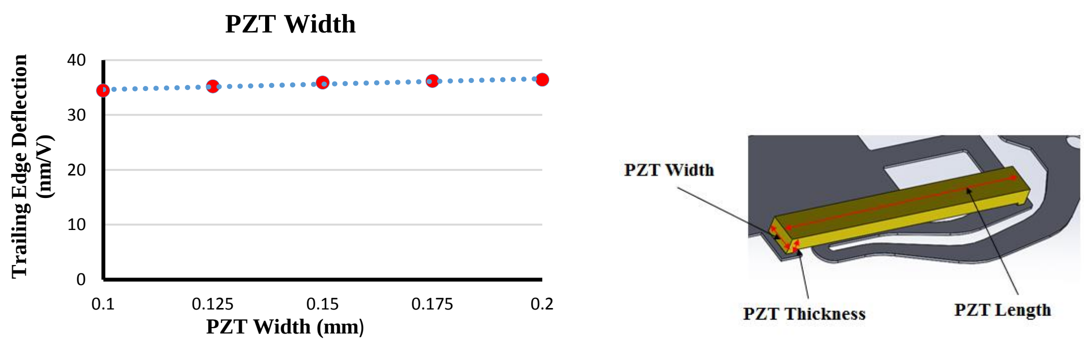

Figure 30: Lateral deflection as a function of **a)** PZT length (upper left), **b)** PZT thickness (upper right), **c)** PZT width (lower left), continued

4.1.2 Gimbal Parameters

Three chosen gimbal design parameters and their comparison values are shown in Table 4.

Table 4: Gimbal design parameters dimensions

Parameter Name	Value (mm)
Neck Length	0.58, 0.60, *0.62*, 0.64, 0.66
Neck Width	0.10, 0.12, *0.14*, 0.16, 0.18
Tongue Thickness	0.014, 0.018, *0.018*, 0.020, 0.022

In Figure 31a and Figure 31b, the lateral deflection of the trailing edge is plotted as a function of neck length and neck width, respectively. Figure 31c shows the lateral deflection as a function of the thickness of the tongue. We observe that neck length, neck width, and tongue thickness have a very small effect on the lateral deflection for the chosen range. The reason for this unexpected result is that the change of stiffness of the neck is negligible compared to the PZT stiffness.

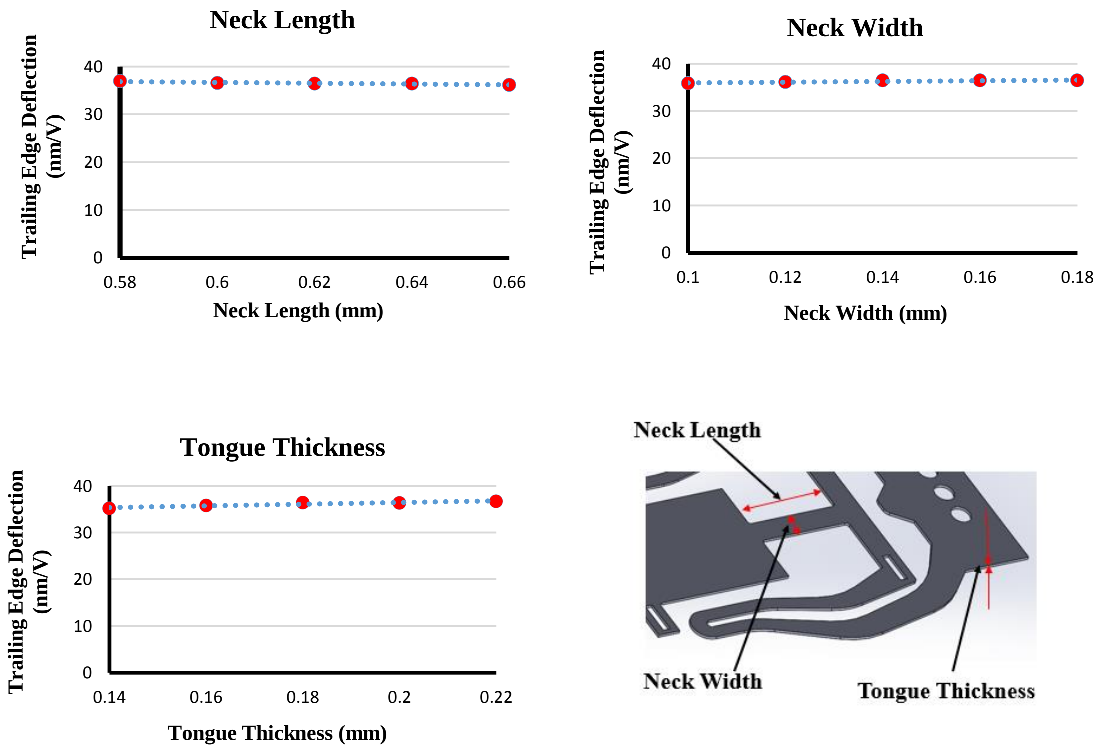

Figure 31: Lateral deflection as a function of **a)** neck length (upper left), **b)** neck width (upper right), **c)** tongue thickness (lower left).

4.1.3 Polyimide Ring Parameters

Two polyimide ring design parameters and their comparison values are shown in Table 5.

Table 5: Polyimide ring design parameters dimensions

Parameter Name	**Value (mm)**
PI Width	0.05, 0.075, *0.10*, 0.125, 0.15
PI Thickness	0.005, 0.0075, *0.010*, 0.0125, 0.015

When the read-write head is flying above the disk, the polyimide ring adds stiffness during shock. Also it provides support for the copper traces as a base material.

In Figure 32a and Figure 32b, the lateral deflection is shown as a function of the polyimide ring thickness and polyimide ring width, respectively. The lateral deflection decreases with an increase in polyimide thickness and width. Clearly, an increase in the stiffness of the polyimide ring decreases the lateral deflection.

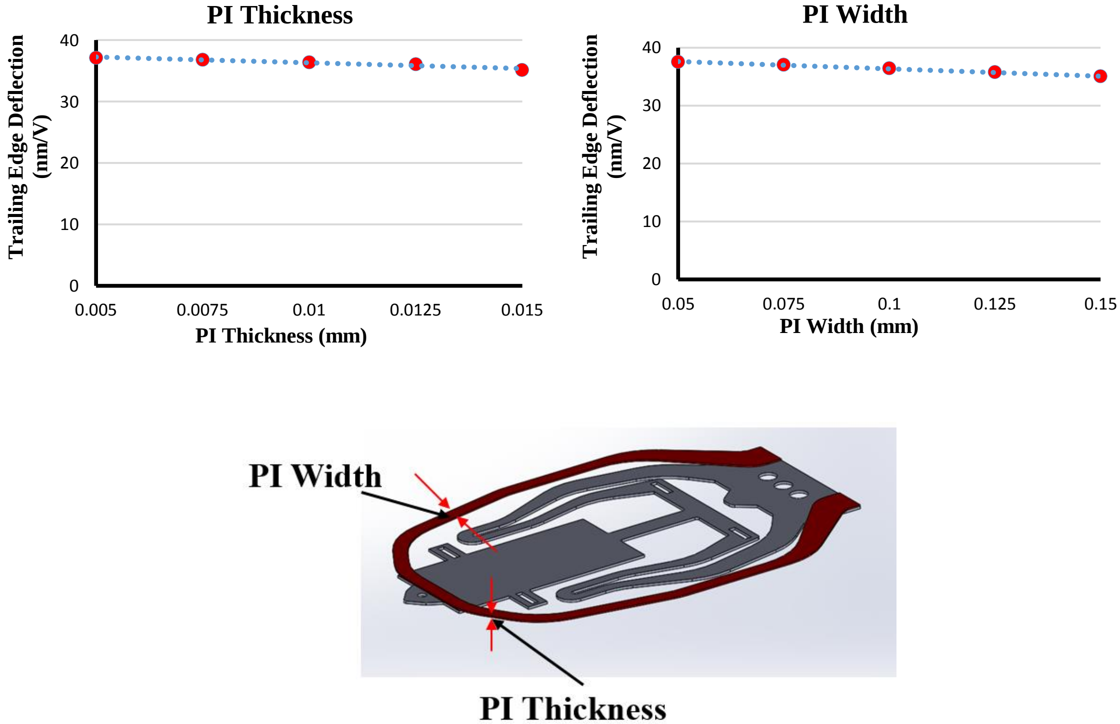

Figure 32: Lateral deflection as a function of **a)** PI thickness (upper left), **b** PI width (upper right).

4.1.4 Arm Parameters

Both “arm” design parameters and their comparison values are shown in Table 6.

Table 6: Arm design parameters

Parameter Name	Value (mm)
Arm Length	0.15, 0.19, *0.23*, 0.27, 0.31
Arm Width	0.06, 0.07, *0.08*, 0.09, 0.10

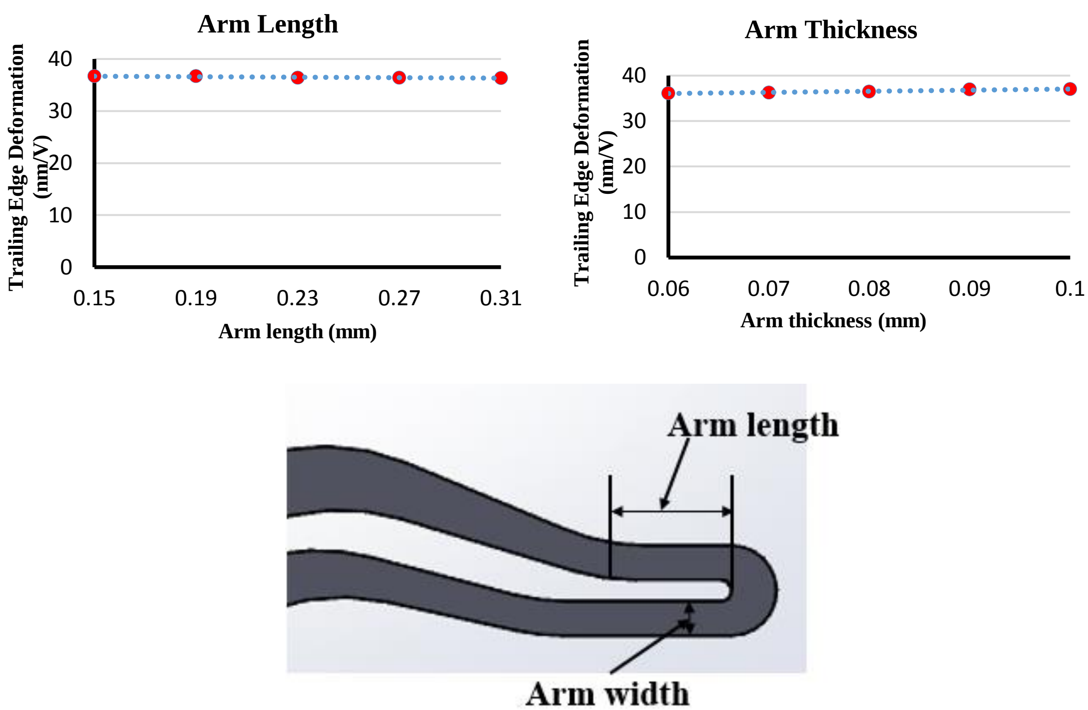

Figure 33: Lateral deflection as a function of **a)** Arm length (upper left), **b)** Arm width (upper right).

In Figure 33, the lateral deflection is shown as a function of the arm length and arm width, respectively. We observe that arm length and arm width have a marginal effect on the lateral deflection for the chosen range. The reason for this is that the change of stiffness of the arm is negligible compared to the PZT stiffness.

4.2 Response frequencies of the suspensions

A resonant frequency is a natural frequency of vibration determined by the physical parameters of the vibrating object[27]. The majority of structures can be made to resonate, i.e. to vibrate with large oscillatory motion. Resonance is one of the reasons causing vibration and noise related problems that occur in structures and operating machinery. Modal analysis is a common way to determine the modes of vibration of a structure. The modal modes are determined by the material properties (mass, damping, and stiffness), and by the boundary conditions of the structure. A multiple degree of freedom system can be described as the following equation[28]:

$$\mathbf{M}\ddot{\mathbf{x}}(t)+\mathbf{C}\dot{\mathbf{x}}(t)+\mathbf{K}\mathbf{x}(t)=\mathbf{f}(t), \tag{4.1}$$

where $\mathbf{M}$ is the mass matrix, $\mathbf{C}$ is the damping coefficient matrix, $\mathbf{K}$ is the stiffness matrix, $\mathbf{x}$ is the displacement, and $\mathbf{f}$ is the external force matrix.

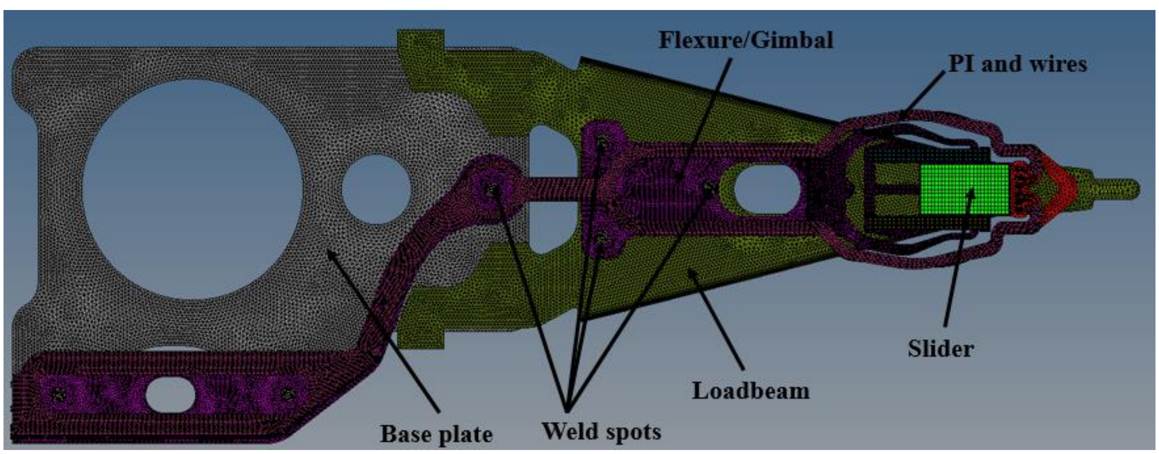

Figure 34: Meshed whole suspension

To investigate the dynamic characteristics of the collocated suspension, we calculated the resonance frequencies for bending, torsion and sway modes using FEA software. The whole suspension was discretized with HyperMesh. The PZTs and the slider were meshed with 3D brick elements due to their rectangular shapes. Because of the small thickness, the flexure, loadbeam, base plate, PI, and wires were meshed with shell elements. The loadbeam, the base plate and PI were connected with weld spots.

Table 7 shows the comparison of the frequencies for a conventional single stage actuator, a suspension-based DSA and a collocated DSA. We observe that the 1st bending, 2nd bending and 1st torsional frequencies of the collocated DSA are slightly higher than those of the SSA and suspension-based DSA. However, the 2nd torsional frequency of the collocated DSA is much smaller than that of the two other designs, which might be due to the fact that the location of the two PZTs is close to the head. The sway mode frequency of the collocated design is slightly smaller than that of the SSA as well.

Table 7: Frequency response

Mode type	**Conventional SSA (kHz)**	**Suspension-based DSA (kHz)**	**Collocated DSA (kHz)**
1st bending	5.59	6.48	7.15
2nd bending	10.26	12.23	13.06
1st torsion	11.50	11.58	12.35
2nd torsion	17.05	17.33	12.40
Sway	24.99	21.66	22.77

The dimensions of the PZT used in this modal analysis are 1.75mm*0.20mm*0.10mm. Other PZT dimensions (1.75mm*0.20*0.05mm and

1.75mm*0.10mm*0.10mm) have also been evaluated, shown in Figure 35. We observe slightly smaller frequencies (within 10%) for both cases due to the reduction of stiffness.

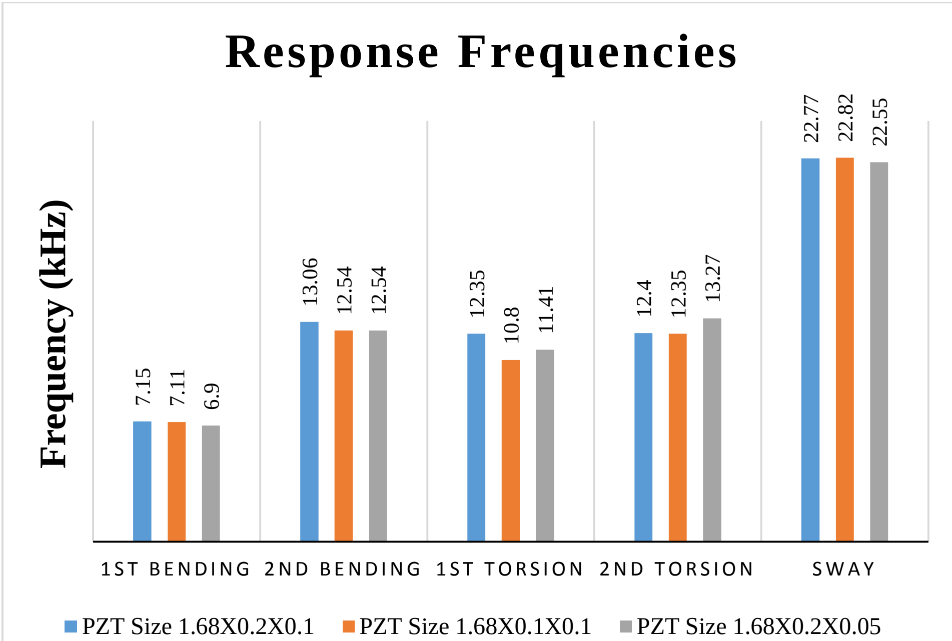

Figure 35: Frequency response for suspensions with different PZT sizes

4.3 Stress Distribution

Figure 36 and Figure 37 show the Von-Mises stress distribution of the dual stage actuator HGA. A maximum Von-Mises stress of 0.53MPa was obtained for an unconstrained dimple and 0.65MPa for a constrained dimple. The gimbal is made of stainless steel with a yield strength of 250 MPa. The PZT dimensions have the greatest influences on changing the trailing edge deformation. Thus they have the same trend on affecting the stress changing.

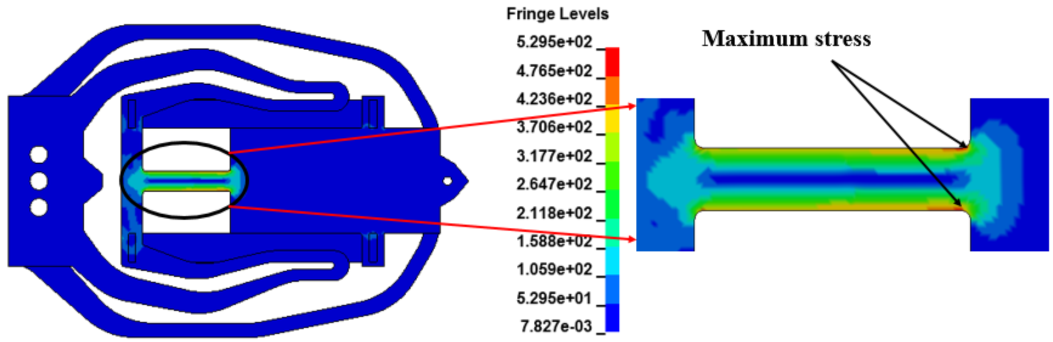

Figure 36: Von-Mises stress distribution of the “base-model” HGA

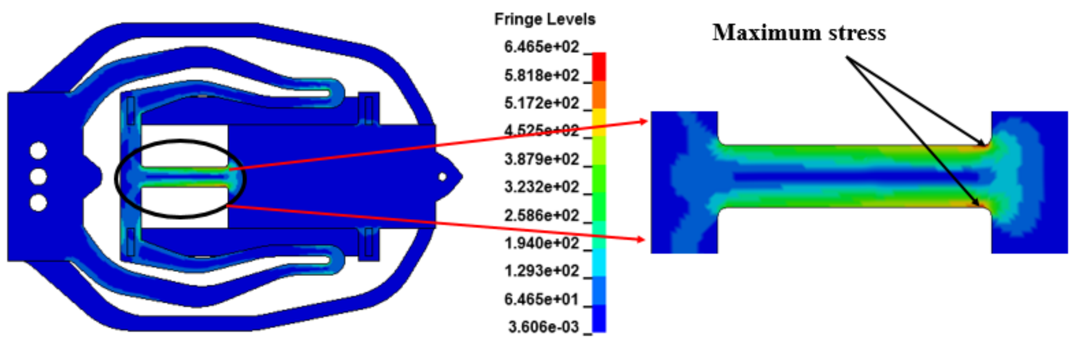

Figure 37: Von-Mises stress distribution of the “base-model” HGA with a constraint at dimple location

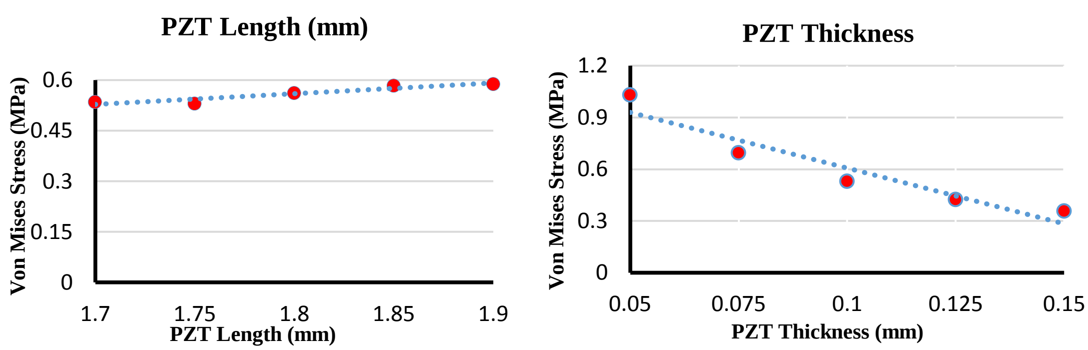

Figure 38: Von-Mises stress as a function of **a)** PZT length, **b)** PZT thickness, **c)** PZT width

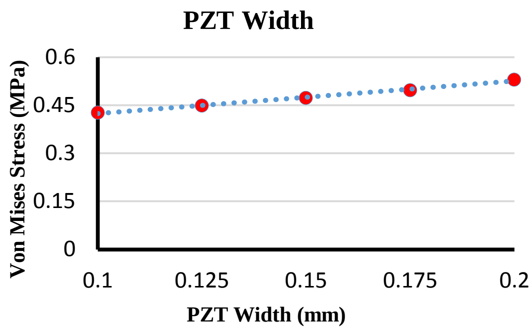

Figure 38: Von-Mises stress as a function of **a)** PZT length, **b)** PZT thickness, **c)** PZT width, continued

The stress comparison study was conducted for the unstrained dimple case. In Figure 38, the Von-Mises stress is plotted as a function of the PZT length, PZT height and PZT width, respectively. The results follows the same trend as the trailing edge lateral deflection. We observe that the stress decreases from 1 MPa to 0.4 MPa as the PZT thickness increases from 0.05mm to 0.15mm. A slight increase in the stress is observed if the PZT becomes longer and wider. For the PZT with dimensions 1.75mm*0.20*0.05mm, the maximum stress observed is 1.03 MPa, which is much smaller than the material yield strength of 250 MPa. The designs can be considered to be very robust.

4.4 Discussion

The main goal of the collocated DSA design in this paper is to increase the trailing edge lateral deflection for a voltage input to the PZT. In Lengert's previous study, the lateral deflection of a typical suspension-based DSA was found to be on the order of

20nm/V, while the single piece PZT collocated DSA design was on the order of 3 to 5nm/V. In this paper, the lateral deflection for the push-pull collocated DSA design was found to be on the order of 30nm/V without a dimple constraint, or on the order 10nm/V with a dimple constraint. This paper investigated optimization for the individual design parameters one at a time. Among the design parameters, the thickness of the PZT plays the most essential role in effecting the magnitude of the lateral deflection.

The stroke of the collocated DSA can be optimized to achieve the requirement of improving track performance. A true optimal design can be obtained by defining a cost function and changing all design parameters simultaneously while minimizing the function keeping maximum stress and the frequency response in a permissible range. In this case, the most important control variables are PZT length, PZT thickness, PZT width, PI thickness, and PI width.

4.5 Acknowledgement

Chapter 4, in part, is a reprint of the material as it appears in “Design and Optimization of Collocated Dual Stage Suspensions”, Yangfan Wang, Longqiu Li, Karcher Morris, John Hogan, Frank E. Talke, submitted to Microsystem Technologies, 2014.

5 Conclusions and Future Perspectives

Chapter 5 summarizes the thesis and presents the collocated DSA current encountered problems.

5.1 Conclusions

In the year 2015, a single 3.5” form factor personal HDD has reached 8 TB. With nearly 60 years of evolution, the areal density of HDDs has increased by 500 million folds.

This paper investigates the lateral deflection of a flexure-based collocated dual stage actuator using commercial finite element software HyperMesh and Ls-Dyna. Model discretization, boundary conditions, and interface contact methods are well illustrated. PZT deformation is simulated using a thermal analogy.

David Lengert’s work of suspension-based DSAs and collocated single piece PZT DSAs are studied and used as comparisons with the newly designed two piece “push-pull” collocated models. By comparing the effect of each design parameter on the lateral deflection, the following conclusions can be drawn:

- The PZT thickness has a large impact on lateral deflection due to the working principle of piezoelectricity. The lateral deformation is inversely proportional to PZT thickness. As the PZT increases in width and length, an increase is found in trailing edge lateral deflection due to the increased stiffness of the PZTs.

- The stiffness of neck length, neck width, and tongue thickness are negligible compared to the PZT stiffness. They have a small effect on the lateral deflection in the chosen range.
- The purpose of the polyimide ring is for added stiffness during flying and during shock. The polyimide ring also provides a base and protection for electric wires from the suspension to the read/write element in the air bearing slider. The lateral deflection is inversely proportional to polyimide thickness and width.
- The stiffness of arm length and width are small compared to the PZT stiffness. They have a small effect on the lateral deflection.
- Resonance frequencies of the collocated design are found to be generally higher than the resonance frequencies found in Lengert's suspension-based DSA except for the second torsional frequency.
- Suspension arms with different PZT sizes have been evaluated, showing slightly smaller frequencies (within 10%) for both cases compared to the base model due to reduction of stiffness.
- The Von-Mises stresses are evaluated for various PZT dimensions. The results followed the same trend as the trailing edge lateral deflection. The stress ranges from 0.4 MPa to 1.1 MPa, which can be considered very robust.
- This paper investigated optimization for the individual design parameters one at a time. A "global" optimal design can be obtained by defining a cost function and changing all design parameters simultaneously while minimizing the function keeping maximum stress and the frequency response to be adequate.

5.2 Future Perspectives

One problem that suspension companies have encountered is the mechanical integrity of the collocated DSA during shock test. When HDDs are dropped and encounter very high G load, it has been observed that PZTs may fracture and/or separate from the suspension. One of the contributing factors to this result includes the amount and the shape of the adhesive layers between the PZTs and mounting surfaces. Fracture of the PZTs is promoted by their brittle material properties. A promising way to overcome this is to use a multi-layer structure shown in Figure 39. The two half “shelf” conductive material parts are applied with a voltage across them. The active layers are PZT materials while the non-active layers can be PZT material or a different material to improve the structural integrity of the element as a whole. One can utilize FEA software to simulate the multi-layer PZTs, the adhesive layers, and the shock test. Additional components with specific material properties should be considered in the HGA model, including details of the wiring, the solder spots, the weld spots, and the adhesive layer between different components.

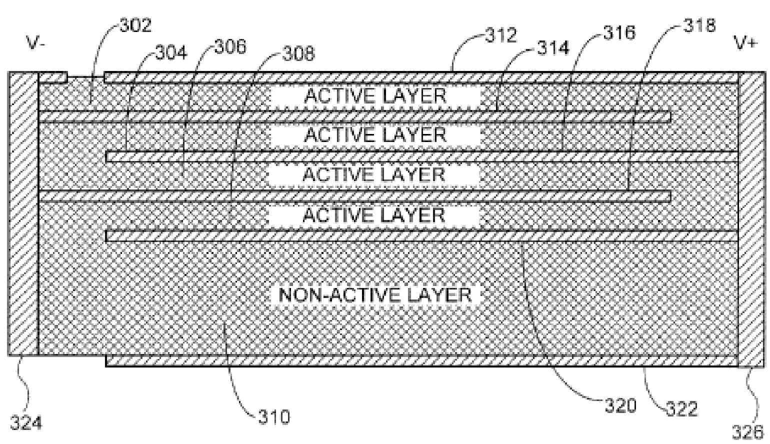

Figure 39: Multi-layer piezoelectric transducer with inactive layers[29]

Bibliography

[1] D. Lengert, E. B. Fanslau, and F. E. Talke, "Design of suspension-based and collocated dual stage actuated suspensions," *Microsyst. Technol.*, vol. 18, pp. 1615–1622, 2012.

[2] IBM Corporation, "http://www.ibm.com/."

[3] Seagate Technology, "http://www.seagate.com/."

[4] B. Marchon, T. Pitchford, Y. T. Hsia, and S. Gangopadhyay, "The head-disk interface roadmap to an areal density of 4 Tbit/in 2," *Adv. Tribol.*, vol. 2013, no. Figure 2, 2013.

[5] Western Digital Technologies, "http://www.wdc.com/."

[6] Hitachi Global Storage Technologies, "http://www.hgst.com/."

[7] M. Kurita, J. Xu, M. Tokuyama, K. Nakamoto, S. Saegusa, and Y. Maruyama, "Flying-height reduction of magnetic-head slider due to thermal protrusion," *IEEE Trans. Magn.*, vol. 41, no. 10, pp. 3007–3009, 2005.

[8] P. A. Salas and F. E. Talke, "Numerical simulation of thermal flying-height control sliders to dynamically minimize flying height variations," *IEEE Trans. Magn.*, vol. 49, no. 4, pp. 1337–1342, 2013.

[9] U. Boettcher, H. Li, R. a. De Callafon, and F. E. Talke, "Dynamic flying height adjustment in hard disk drives through feedforward control," *IEEE Trans. Magn.*, vol. 47, no. 7, pp. 1823–1829, 2011.

[10] Hutchinson Technology, "http://www.htch.com/."

[11] O. Reynolds, "An experimental investigation of the circumstances which determine whether the motion of water shall be direct or sinous: And of the law of resistance in parallel channels," *R. Soc. London*, vol. 4, no. 1883, p. 438, 1967.

[12] R. C. Tseng, "Rarefaction Effects of Gas-Lubricated Bearings in a Magnetic Recording Disk File," *J. Lubr. Technol.*, vol. 97, no. October, p. 624, 1975.

[13] Y.-T. Hsia and G. a. Domoto, "An Experimental Investigation of Molecular Rarefaction Effects in Gas Lubricated Bearings at Ultra-Low Clearances," *J. Lubr. Technol.*, vol. 105, no. January, p. 120, 1983.

[14] M. Duwensee, "Numerical and experimental investigations of the head/disk interface," Thesis, University of California, San Diego, 2007.

[15] R. Brunner, “Properties of Carbon Overcoates and Perfluoro-polyether Lubricants in Hard Disk Drives,” Thesis, University of California, San Diego, 2009.

[16] H. J. Richter, A. Y. Dobin, K. Gao, O. Heinonen, R. J. Van de Veerdonk, R. T. Lynch, D. K. Xue, J.WEller, P. Asselin, and M. F. E. and R. M. Brockie, “Recording on bit-patterned media at densities of 1Tb/in 2 and beyond.,” *IEEE Trans. Mag.*, vol. 38, pp. 2255–2260, 2006.

[17] K. Mori, T. Munemoto, H. Otsuki, Y. Yamaguchi, and K. Akagi, “A dual-stage magnetic disk drive actuator using a piezoelectric device for a high track density,” *IEEE Trans. Magn.*, vol. 27, no. 6, pp. 5298–5300, 1991.

[18] G. Gautschi, “Force, Strain, Pressure, Acceleration and Acoustic Emission Sensors, Materials and Amplifiers.,” in *Piezoelectric Sensorics*, 2002.

[19] Piezo System Inc, “http://www.piezo.com/.”

[20] R. B. Evans, J. S. Griesbach, and W. C. Messner, “Piezoelectric microactuator for dual stage control,” *IEEE Trans. Magn.*, vol. 35, no. 2, pp. 977–982, 1999.

[21] G. K. Lau and H. Du, “A piezoelectric quad-morph actuated suspension for hard disk drives,” *J. Micromechanics Microengineering*, vol. 16, pp. 1833–1840, 2006.

[22] U. Boettcher, B. Raeymaekers, R. a. De Callafon, and F. E. Talke, “Dynamic modeling and control of a piezo-electric dual-stage tape servo actuator,” *IEEE Trans. Magn.*, vol. 45, no. Ldv, pp. 3017–3024, 2009.

[23] Y. Liu, X. Wang, and Y. Lu, “Circuit model for piezoelectric actuator with electrically conductive epoxy,” pp. 1559–1565, 2013.

[24] Y. Liu, “Analytical dynamic model for suspension with PZT actuators,” *Microsyst. Technol.*, vol. 19, pp. 1269–1274, 2013.

[25] Y. Jing, J. Luo, P. Huang, and L. Qin, “U-type piezoelectric thin-film microactuator for hard disk drives,” *IEEE Trans. Magn.*, vol. 41, no. 11, pp. 4309–4314, 2005.

[26] T. Hughes, *The finite element method: linear static and dynamic finite element analysis*. .

[27] Hyper Physics, “http://hyperphysics.phy-astr.gsu.edu/.”

[28] J. He and Z.-F. Fu, “Modal Analysis,” *Modal Anal.*, vol. 117, p. 291, 2001.

[29] J. Wright and R. Zambri, “Multi-layer Piezoelectric Transducer With Inactive Layers,” US20140104722A1, 2012.